arXiv:1703.10302v1 [quant-ph] 30 Mar 2017

10-qubit entanglement and parallel logic operations with a superconducting circuit

Chao Song[1,2],* Kai Xu[1,2],* Wuxin Liu[1], Chuiping Yang[3], Shi-Biao Zheng[4],† Hui Deng[5], Qiwei Xie[6], Keqiang Huang[5], Qiujiang Guo[1], Libo Zhang[1], Pengfei Zhang[1], Da Xu[1], Dongning Zheng[5], Xiaobo Zhu[2],‡ H. Wang[1,2],§ Y.-A. Chen[2], C.-Y. Lu[2], Siyuan Han[7], and J.-W. Pan[2]

[1]*Department of Physics, Zhejiang University, Hangzhou, Zhejiang 310027, China,*
[2]*Synergetic Innovation Center of Quantum Information and Quantum Physics, University of Science and Technology of China, Hefei, Anhui 230026, China,*
[3]*Department of Physics, Hangzhou Normal University, Hangzhou, Zhejiang 310036, China,*
[4]*Fujian Key Laboratory of Quantum Information and Quantum Optics, College of Physics and Information Engineering, Fuzhou University, Fuzhou, Fujian 350116, China,*
[5]*Institute of Physics, Chinese Academy of Sciences, Beijing 100190, China,*
[6]*Institute of Automation, Chinese Academy of Sciences, Beijing 100190, China,*
[7]*Department of Physics and Astronomy, University of Kansas, Lawrence, Kansas 66045, USA*

(Dated: March 31, 2017)

Here we report on the production and tomography of genuinely entangled Greenberger-Horne-Zeilinger states with up to 10 qubits connecting to a bus resonator in a superconducting circuit, where the resonator-mediated qubit-qubit interactions are used to controllably entangle multiple qubits and to operate on different pairs of qubits in parallel. The resulting 10-qubit density matrix is unambiguously probed, with a fidelity of 0.668 ± 0.025. Our results demonstrate the largest entanglement created so far in solid-state architectures, and pave the way to large-scale quantum computation.

Entanglement is one of the most counter-intuitive features of quantum mechanics. The creation of increasingly large number of entangled quantum bits (qubits) is central for measurement-based quantum computation [1], quantum error correction [2, 3], quantum simulation [4], and foundational studies of nonlocality [5, 6] and quantum-to-classical transition [7]. A significant experimental challenge for engineering multiqubit entanglement [8–10] has been noise control. With solid-state platforms, the largest number of entangled qubits reported so far is five [10], and further scaling up would be difficult as constrained by the qubit coherence and the employed sequential-gate method.

Superconducting circuits are a promising solid-state platform for quantum state manipulation and quantum computing owing to the microfabrication technology scalability, individual qubit addressability, and ever-increasing qubit coherence time. The past decade has witnessed significant progresses in quantum information processing and entanglement engineering with superconducting qubits: preparation of three-qubit entangled states [11, 12], demonstration of elementary quantum algorithms [13, 14], realization of three-qubit Toffoli gates and quantum error correction [15, 16]. In particular, a recent experiment has achieved a two-qubit controlled-phase gate with a fidelity above 99 percent with a superconducting quantum processor [10], where five transmon qubits with nearest-neighbor coupling are arranged in a linear array. Based on this gate, a five-qubit Greenberger-Horne-Zeilinger (GHZ) state was produced step by step; the number of entangled qubits is increased by one at a time.

In this letter we demonstrate a versatile superconducting quantum processor featuring high connectivity with programmable qubit-qubit couplings mediated by a bus resonator, and experimentally produce GHZ states with up to 10 qubits using this quantum processor. The resonator-induced qubit-qubit couplings result in a phase shift that is quadratically proportional to the total qubit excitation number, evolving the participating qubits from an initially product state to the GHZ state after a single collective interaction, irrespective of the number of the entangled qubits [17]. We characterize the multipartite entanglement by quantum state tomography achieved by synchronized local manipulations and detections of the entangled qubits, and measure a fidelity of 0.668 ± 0.025 for the 10-qubit GHZ state, which confirms the genuine tenpartite entanglement [18] with 6.7 standard deviations (σ). We also implement parallel entangling operations mediated by the resonator, simultaneously generating three Einstein-Podolsky-Rosen (EPR) pairs; this feature was previously suggested in the context of ion traps [19] and quantum dots coupled to an optical cavity [20], but experimental demonstrations are still lacking.

The superconducting quantum processor is illustrated in Fig. 1(a), which is constructed as 10 transmon qubits (Q_j for $j = 1$ to 10), with resonant frequencies $\omega_j/2\pi$ tunable from 5 to 6 GHz, symmetrically coupled to a central resonator (B), whose resonant frequency is fixed at $\omega_B/2\pi \approx 5.795$ GHz [21]. Measured qubit-resonator (Q_j-B) coupling strengths $g_j/2\pi$ range from 14 to 20 MHz (see Supplemental Material [22] for details on device, operation, and readout). The central resonator serves as a multipurpose actuator, enabling controlled long-range logic operations, scalable multiqubit entanglement, and quantum state transfer. In the rotating-wave approximation and ignoring the crosstalks between qubits (see Supplemental Material [22]), the Hamiltonian of the sys-

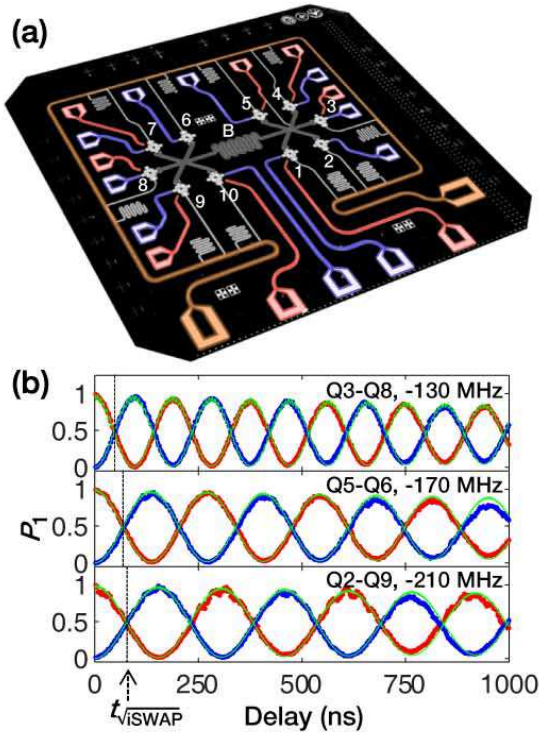

FIG. 1: (a) False-color circuit image showing 10 superconducting qubits (star shapes) interconnected by a central bus resonator B (grey). Each qubit has its own microwave line (red) for xy control and flux bias line (blue) for z control, except for Q_2 and Q_6, which share the microwave lines of neighboring qubits. Each qubit has its own readout resonator, which couples to the circumferential transmission line (orange) for simultaneous readout. (b) Parallel intra-pair SE interactions for Q_3-Q_8 (top), Q_5-Q_6 (middle), and Q_2-Q_9 (bottom) at the corresponding detunings as indicated. The anti-correlated, time-modulated occupation probabilities P_{10} (red dots) and P_{01} (blue dots) of each pair indicate that energy is exchanged within the pair [6], undisturbed by what happen in the other two pairs: 6 qubits in three pairs are measured simultaneously and we trace out the other pairs' indices for the data in each panel. Lines (green) are numerical simulations.

tem is given by

$$H/\hbar = \omega_B a^+ a + \sum_{j=1}^{10} \left[\omega_j |1_j\rangle\langle 1_j| + g_j(\sigma_j^+ a + \sigma_j^- a^+)\right], \tag{1}$$

where σ_j^+ (σ_j^-) is the raising (lowering) operator of Q_j and a^+ (a) is the creation (annihilation) operator of B.

The qubit-qubit coupling can be realized through the superexchange (SE) interaction [23] mediated by the bus resonator B [24–26]. With multiplexing we can further arrange multiple qubit pairs at different frequencies to turn on the intra-pair SE interactions simultaneously. To illustrate this feature, we consider three qubit pairs, Q_k-$Q_{k'}$, Q_l-$Q_{l'}$, and Q_m-$Q_{m'}$, detuned from resonator B by Δ_j ($\equiv \omega_j - \omega_B$, and $\omega_j = \omega_{j'}$) for $j = k$, l, and m, respectively, while all other qubits are far detuned and can be neglected for now. In the dispersive regime and when the resonator B is initially in the ground state, it will remain so throughout the procedure and the effective Hamiltonian for the qubit pairs is

$$H_1/\hbar = \sum_{j\in\{k,l,m\}} \lambda_j \left(\sigma_j^- \sigma_{j'}^+ + \sigma_j^+ \sigma_{j'}^-\right) + \sum_{j\in\{k,l,m\}} \left[\frac{g_j^2}{\Delta_j} |1_j\rangle\langle 1_j| + \frac{g_{j'}^2}{\Delta_j} |1_{j'}\rangle\langle 1_{j'}|\right], \tag{2}$$

where $\lambda_j = \frac{g_j g_{j'}}{\Delta_j}$, $|\Delta_j| \gg g_j, g'_j$, and $|\Delta_{j_1} - \Delta_{j_2}| \gg \lambda_{j_1}, \lambda'_{j_1}, \lambda_{j_2}, \lambda'_{j_2}$ for $j_1, j_2 \in \{k, l, m\}$ and $j_1 \neq j_2$. With this setting, the resonator B is simultaneously used for three intra-pair SE processes; the inter-pair couplings are effectively switched off due to large detunings between different pairs.

With the fast z control on each qubit, coupling between any two qubits can be dynamically turned on and off by matching (intra-pair) and detuning (inter-pair), respectively, their frequencies, i.e., we can reconfigure the coupling structure in-situ without modifying the physical wiring of the circuit. For example, by arranging Δ_k, Δ_l, and Δ_m in Eq. (2) at three distinct frequencies, we create three qubit pairs (Q_2-Q_9, Q_3-Q_8, and Q_5-Q_6) featuring programmable intra-pair SE interactions with negligible inter-pair crosstalks, enabling parallel couplings as demonstrated in Fig. 1(b). According to the probability evolutions shown in Fig. 1(b), a characteristic gate time, $t_{\sqrt{\text{iSWAP}}}$, for each qubit pair can be be identified [6].

Operating multiple pairs in parallel naturally produces multiple EPR pairs [24, 25]. As the pulse sequence shows in Fig. 2(a), three EPR pairs are produced after the completion of all three SE-$\sqrt{\text{iSWAP}}$ gates, with the 6-qubit quantum state tomography measuring an overall state fidelity of 0.904 ± 0.018. The inferred density matrix ρ is validated by satisfying the physical constraints of Hermitian, unit trace, and positive semi-definite. We further perform partial trace on ρ to obtain three 2-qubit reduced density matrices, each corresponding to a EPR pair with a fidelity above 0.93 (Fig. 2(b)).

Remarkably, our architecture allows high-efficiency generation of multiqubit GHZ states. In contrast to the previous approach where GHZ states are generated by a series of controlled-NOT (CNOT) gates [10], here all the qubits connected to the bus resonator can be entangled with a single collective qubit-resonator interaction. In the theoretical proposal [17, 27], N qubits are assumed to be equally coupled to the resonator and are detuned from the resonator by the same amount Δ that is much larger than the qubit-resonator coupling. When all qubits are initialized in the same equal superpositions of $|0\rangle$ and $|1\rangle$, e.g., $(|0\rangle - i|1\rangle)/\sqrt{2}$, the SE interaction does not induce any energy exchange between qubits; instead, it produces a dynamic phase that nonlinearly depends upon the collective qubit excitation num-

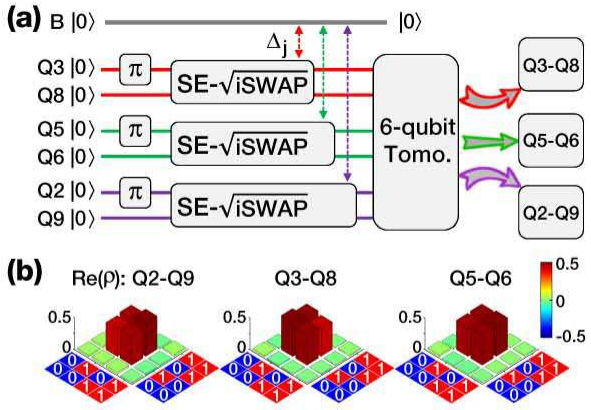

FIG. 2: (a) Pulse sequence with detunings listed in Fig. 1(b). Tomography is performed to reconstruct the 6-qubit density matrix, over which we perform partial trace to obtain the reduced density matrix of each EPR pair. (b) Real parts of the reconstructed 2-qubit density matrices for the three EPR pairs of Q_2-Q_9, Q_3-Q_8, and Q_5-Q_6, with fidelities (concurrences) of 0.932 ± 0.13 (0.869 ± 0.026), 0.957 ± 0.010 (0.915 ± 0.019), and 0.951 ± 0.010 (0.909 ± 0.019), respectively. For clarity of display, single-qubit z-axis rotations are numerically applied to Q_2 (93°), Q_3 (165°), and Q_5 (42°) to cancel the arguments of the major off-diagonal elements.

ber k as $k(N+1-k)\theta$, where θ is determined by the effective qubit-qubit coupling strength and the interaction time. With the choice $\theta = \pi/2$, this gives rise to the GHZ state $\left(|+_1, +_2, ..., +_N\rangle + i|-_1, -_2, ..., -_N\rangle\right)/\sqrt{2}$, where $|\pm_j\rangle = \left(|0_j\rangle \pm i^N |1_j\rangle\right)/\sqrt{2}$ [17].

Here we apply this proposal to our experiment. We find that, though the qubit-resonator couplings are not uniform and unwanted crosstalk couplings exist in our circuit, we can optimize each qubit's detuning and the overall interaction time to achieve GHZ states with high fidelities as guided by numerical simulation. The pulse sequence is shown in Fig. 3(a). We start with initializing the chosen N qubits in $\left(|0\rangle - i\,|1\rangle\right)/\sqrt{2}$ by applying $\pi/2$ pulses at their respective idle frequencies, following which we bias them to nearby $\Delta/2\pi \approx -140$ MHz for an optimized duration of approximately twice $t_{\sqrt{\text{iSWAP}}}$. The phase of each qubit's xy drive is calibrated according to the rotating frame with respect to Δ, ensuring that all N qubits are in the same initial state just when their SE interactions are switched on [22, 28]. After the optimized interaction time, these qubits approximately evolve to the GHZ state $|\Psi_1\rangle = \left(|+_1, +_2, ..., +_N\rangle + e^{i\varphi}|-_1, -_2, ..., -_N\rangle\right)/\sqrt{2}$, where φ may not be equal to $\pi/2$ as in the ideal case with uniform qubit-qubit interactions; however, this phase variation does not affect entanglement. Later on we bias these N qubits back to their idle frequencies; during the process a dynamical phase ϕ_j is accumulated between $|0\rangle$ and $|1\rangle$ of Q_j. Re-defining $|\pm_j\rangle = \left(|0_j\rangle \pm i^N e^{i\phi_j} |1_j\rangle\right)/\sqrt{2}$ ensures that the above-mentioned formulation of $|\Psi_1\rangle$ remains invariant, which is equivalent to a z-axis rotation of the x-y-z reference frame, i.e., $x \to x'$ and $y \to y'$. Tracking the new axes is important for characterization of the produced GHZ states.

Tomography of the produced states requires individually measuring the qubits in bases formed by the eigenvectors of the Pauli operators X, Y, and Z, respectively. Measurement in the Z basis can be directly performed. For each state preparation and measurement event, we record the 0 or 1 outcomes of each qubit and do so for N qubits simultaneously; repeating the state preparation and measurement event thousands of times we count 2^N probabilities of $\{P_{00...0}, P_{00...1}, ..., P_{11...1}\}$. Measurement in the X (Y) basis is achieved by inserting a Pauli Y (X) rotation on each qubit before readout. All together, the 3^N tomographic operations and the 2^N probabilities for each operation allow us to unambiguously reconstruct all elements of the density matrix ρ (see Supplemental Material [22] for various aspects of our tomography technique including measurement stability, reliability with reduced sampling size, and pre-processing for minimizing the computational cost). The resulting 10-qubit GHZ density matrix is partially illustrated in Fig. 3(b), with a fidelity of 0.668 ± 0.025, and the N-qubit GHZ fidelity as function of N is plotted in Fig. 3(b) inset. The achieved fidelities are well above the threshold for genuine multipartite entanglement [18].

The full tomography technique, though general and accurate, is costly when N is large. The produced GHZ states can also be characterized by a shortcut, since the ideal GHZ density matrix consists of only four non-zero elements in a suitably chosen basis. To do so, we apply to each qubit a $\pi/2$ rotation around its y' or x' axis, transforming $|\Psi_1\rangle$ to $|\Psi_2\rangle = \left(|00...0\rangle + e^{i\varphi}|11...1\rangle\right)/\sqrt{2}$ (here and below we omit the subscripts of the qubit index for clarity). The diagonal elements $\rho_{00...0}$ and $\rho_{11...1}$ can be directly measured; the off-diagonal elements $\rho_{00...0,\,11...1}$ and $\rho_{11...1,\,00...0}$ can be obtained by measuring the system parity, defined as the expectation value of the operator $P(\gamma) = \otimes_{j=1}^{N}(\cos\gamma Y'_j + \sin\gamma X'_j)$, which is given by $\langle P(\gamma)\rangle = 2\,|\rho_{00...0,\,11...1}|\cos(N\gamma + \varphi)$ for $|\Psi_2\rangle$ [9]. The oscillation patterns of the measured parity as functions of γ confirm the existence of coherence between the states $|00...0\rangle$ and $|11...1\rangle$ (Fig. 3(c)). The fidelity of the N-qubit GHZ state $|\Psi_2\rangle$ can be estimated using the four non-zero elements, which is 0.660 ± 0.020 for $N = 10$. This value agrees with that of the GHZ state $|\Psi_1\rangle$ obtained by full state tomography.

A key advantage of the present protocol for generating GHZ states is its high scalability as demonstrated in Fig. 3(b). If limited by decoherence, the achieved fidelity based on the sequential-CNOT approach, $F_{\text{N,C}}$, scales approximately as $F_{\text{N,C}} \propto F_{2,C}^{N^2/2}$ at large N (see the red dashed line in Fig. 3(b) inset), while that based on our protocol scales as $F_{\text{N}} \propto F_2^N$ (blue dashed line). Here

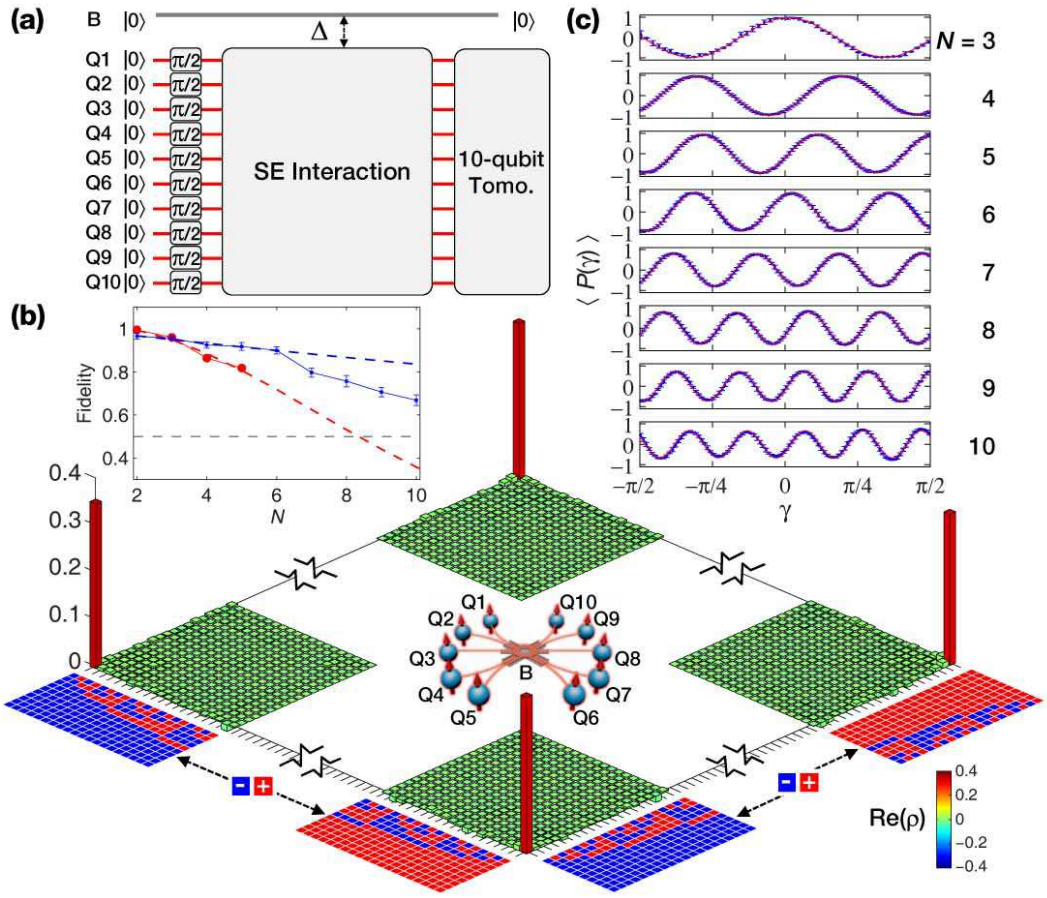

FIG. 3: (a) Pulse sequence for the 10-qubit GHZ state with $\Delta/2\pi \approx -140$ MHz. (b) Partial elements of the measured 10-qubit density matrix, with a fidelity of 0.668 ± 0.025 relative to the ideal GHZ state $|\Psi_1\rangle = \left(|+_1,+_2,...,+_N\rangle + e^{i\varphi}|-_1,-_2,...,-_N\rangle\right)/\sqrt{2}$. For clarity of display, here a single-qubit rotation around the x' axis by an angle of φ is numerically applied to one of the qubit, which cancels the arguments of the dominant off-diagonal elements. Center inset: Cartoon illustration showing 10 entangled qubits. Top-left inset: Experimentally measured GHZ fidelity (blue dots) and the data adapted from Ref. [10] (red dots) as functions of the qubit number N. Error bars are 1σ. Blue and red dashed lines are guides of different error trends. (c) Parity oscillations observed for the N-qubit GHZ states $|\Psi_2\rangle$ defined as superpositions of the basis states $|0_1,0_2,...,0_N\rangle$ and $|1_1,1_2,...,1_N\rangle$ with $N = 3$ to 10. The fringe amplitudes are 0.964 ± 0.016, 0.956 ± 0.018, 0.935 ± 0.020, 0.926 ± 0.026, 0.796 ± 0.023, 0.782 ± 0.025, 0.729 ± 0.028 and 0.660 ± 0.032 from top to bottom. For $N = 10$, the state preparation and measurement sequence is repeated 81,000 times for a sample size large enough to count the 2^N probabilities.

$F_{2,C}$ (F_2) is quoted as the decoherence-limited fidelity of the CNOT gate (present protocol) involving two qubits. The falling of the experimental data (blue dots) below the scaling line when $N \geq 6$ is due to the inhomogeneity of g_j and the crosstalk couplings. One can see that, even with the two-qubit gate fidelity as high as 0.994, the coherence performance of the device used in Ref. [10] does not allow generation of 10-qubit GHZ state with fidelity above the genuine entanglement threshold using the sequential-CNOT approach.

In summary, our experiment demonstrates the viability of the multiqubit-resonator-bus architecture for scalable quantum information processing, with essential functions including high-efficiency entanglement generation and parallel logic operations. We deterministically generate the 10-qubit GHZ state, the largest multiqubit entanglement ever created in solid-state systems, which is verified by quantum state tomography for the first time as well. In addition, our approach allows instant *in situ* rewiring of the qubits. These unique features show the great potential of the demonstrated approach for scalable quantum information processing.

Acknowledgments. This work was supported by the National Basic Research Program of China (Grant No. 2014CB921201), the National Natural Science Foundations of China (Grants No. 11434008, No. 11374054, No. 11574380, and No. 11404386), the Fundamental Research Funds for the Central Universities of China (Grant No. 2016XZZX002-01), and the Ministry of Science and Technology of China (Grant No. 2016YFA0301802).

S.H. was supported by NSF (Grant No. PHY-1314861). Devices were made at the Nanofabrication Facilities at Institute of Physics in Beijing, University of Science and Technology in Hefei, and National Center for Nanoscience and Technology in Beijing.

* C. S. and K. X. contributed equally to this work.
† Electronic address: t96034@fzu.edu.cn
‡ Electronic address: xbzhu16@ustc.edu.cn
§ Electronic address: hhwang@zju.edu.cn

[1] R. Raussendorf and H. J. Briegel, Phys. Rev. Lett. **86**, 5188 (2001).
[2] A. R. Calderbank and P. W. Shor, Phys. Rev. A **54**, 1098 (1996).
[3] E. Knill, Nature **434**, 39 (2005).
[4] S. Lloyd, Science **273**, 1073 (1996).
[5] D. M. Greenberger, M. A. Horne, A. Shimony, and A. Zeilinger, Am. J. Phys. **58**, 1131 (1990).
[6] M. Ansmann *et al.*, Nature **461**, 504 (2009).
[7] A. J. Leggett, Rep. Prog. Phys. **71**, 022001 (2008).
[8] X. L. Wang *et al.*, Phys. Rev. Lett. **117**, 210502 (2016).
[9] T. Monz *et al.*, Phys. Rev. Lett. **106**, 130506 (2011).
[10] R. Barends *et al.*, Nature **508**, 500 (2014).
[11] L. DiCarlo *et al.*, Nature **467**, 574 (2010).
[12] M. Neeley *et al.*, Nature **467**, 570 (2010).
[13] L. DiCarlo *et al.*, Nature **460**, 240 (2009).
[14] M. Mariantoni *et al.*, Science **334**, 61 (2011).
[15] A. Fedorov, L. Steffen, M. Baur, and A. Wallraff, Nature **481**, 170 (2012).
[16] M. D. Reed, L. DiCarlo, S. E. Nigg, L. Sun, L. Frunzio, S. M. Girvin, and R. J. Schoelkopf, Nature **482**, 382 (2012).
[17] S. B. Zheng, Phys. Rev. Lett. **87**, 230404 (2001).
[18] O. Gühne and G. Tóth, Phys. Rep. **474**, 1 (2009).
[19] A. Sφrensen and K. Mφlmer, Phys. Rev. Lett. **82**, 1971 (1999).
[20] A. Imamoglu *et al.*, Phys. Rev. Lett. **83**, 4204 (1999).
[21] E. Lucero *et al.*, Nat. Phys. **8**, 719 (2012).
[22] See Supplemental Material for more information on the device performance and the tomography experiment.
[23] S. Trotzky *et al.*, Science **319**, 295 (2008).
[24] S. B. Zheng and G. C. Guo, Phys. Rev. Lett. **85**, 2392 (2000).
[25] S. Osnaghi, P. Bertet, A. Auffeves, P. Maioli, M. Brune, J. M. Raimond, and S. Haroche, Phys. Rev. Lett. **87**, 037902 (2001).
[26] J. Majer *et al.*, Nature **449**, 443 (2007).
[27] G. S. Agarwal, R. R. Puri, and R. P. Singh, Phys. Rev. A **56**, 2249 (1997).
[28] Y. P. Zhong *et al.*, Phys. Rev. Lett. **117**, 110501 (2016).

Supplementary Material for "10-qubit entanglement and parallel logic operations with a superconducting circuit"

DEVICE, CONTROL, AND MEASUREMENT INFORMATION

Device

Our sample is a superconducting circuit consisting of 10 Xmon qubits interconnected by a bus resonator, fabricated with two steps of aluminum deposition as described elsewhere [S1]. There is no crossover layer to connect segments of grounding planes on the circuit chip. Instead, aluminum bonding wires are manually applied as many as possible to reduce the impact of parasitic slotline modes. The bus resonator B is a half-wavelength coplanar waveguide resonator with a resonant frequency fixed at $\omega_B/2\pi \approx 5.795$ GHz, which is measured with all coupling qubits staying in $|0\rangle$ at their respective idle frequencies (see below). The resonator has 10 side arms, each is capacitively coupled to an Xmon qubit with the coupling strength g_j listed in Tab. S1. The Xmon qubit is a variant of the transmon qubit, each with an individual flux line for dynamically tuning its frequency and a microwave drive (Q_2, Q_4, and Q_6 share other qubits' microwave lines in this experiment) for controllably exciting its $|0\rangle \leftrightarrow |1\rangle$ transition. The Xmon qubit reaches its maximum resonant frequency ω_j^0 at the sweetpoint, where it is insensitive to flux noise and exhibits the longest phase coherence time. ω_j^0 for $j = 1$ to 10 in our device are around or slightly above ω_B, whose values are roughly estimated through the flux-biased spectroscopy measurement. In this experiment all qubits are initialized to the ground state $|0\rangle$ at their respective idle frequencies $\omega_j/2\pi$ that spread in the range from 4.96 to 5.66 GHz, corresponding to 840 to 140 MHz below $\omega_B/2\pi$ (Tab. S1), where single-qubit rotations and the qubit-state measurement are performed. For entangling operations we dynamically bias all target qubits from their idle frequencies ω_j to the interaction frequency ω_I for a specified interaction period, following which we bias all these qubits back to their ω_j for measurement. Qubit coherence performance at ω_I can be found in Tab. S1 and in Fig. S1.

XY control

Our instrument has 7 (expendable to more) independent xy signal channels controlled by digital analog converters (DACs): 3 channels are selected to output two tones per channel and the rest 4 channels are programmed to output a single tone per channel, for a total of xy controls with 10 tones targeting 10 qubits. The 10 tones are generated with 10 sidebands mixed with a continuous microwave whose carry frequency is $\omega_c/2\pi = 5.324$ GHz. Microwave leakage is minimized with this standard mixing method as calibrated by the room temperature electronics.

In our setup, Q_1 and Q_2 share Q_1's on-chip xy line

TABLE S1: Qubit characteristics. ω_j^0 is the maximum resonant frequency of Q_j, i.e., the resonant frequency at the qubit's sweetpoint where dephasing is minimum. ω_I is the interaction frequency for qubits to entangle, which is about $2\pi \times 140$ MHz below the resonator frequency ω_B. Qubit coherence parameters including the lifetime $T_{1,j}$, the Ramsey Gaussian dephasing time $T_{2,j}^*$, and the spin echo Gaussian dephasing time $T_{2,j}^{\rm SE}$ of Q_j are measured at ω_I where other qubits are far detuned. ω_j is the idle frequency of Q_j, where the $X/2$ gate for state preparation and the tomographic pulses for qubit measurement are applied. g_j is the coupling strength between Q_j and the resonator B, defined in the interaction Hamiltonian $\hbar g_j(\sigma_j^+ + \sigma_j^-)(a^\dagger + a)$, where σ_j^+ (σ_j^-) is the raising (lowering) operator of Q_j and $a^\dagger$ and a are field operators of resonator B. Fidelity of the $X/2$ gate on Q_j is characterized by RB at its idle frequency ω_j; we also simultaneously run RBs on 8 qubits to characterize the $X/2$ gate fidelities for these 8 qubits. Each qubit is measured through its own readout resonator that connects to a common circumferential transmission line, and ω_j^r is the resonant frequency of Q_j's readout resonator R_j, with the Q_j-R_j coupling strength noted as g_j^r. $\delta\omega_j^m$ is the AC stark shift of Q_j during its measurement, i.e., the qubit frequency shifts downwards from ω_j as its readout resonator R_j becomes populated. The readout pulse is 1 μs-long, and carries 10 tones targeting the 10 readout resonators. n_j^r ($= |\delta\omega_j^m/2\chi_j|$, where χ_j is the dispersive frequency shift of the readout resonator when qubit changes state from $|0\rangle$ to $|1\rangle$) is the maximum average photon number in Q_j's readout resonator R_j as excited by the readout pulse for qubit measurement, which decays at the end of the readout pulse with a leakage rate of κ_j^r for R_j returning to the vacuum state and being ready for the next cycle. $F_{0,j}$ ($F_{1,j}$) is the probability of correctly reading out Q_j in $|0\rangle$ ($|1\rangle$) when it is prepared in $|0\rangle$ ($|1\rangle$), which are used to correct the measured qubit probabilities [S2]. Q_3's readout fidelities apply to the entangling experiments with $N \leq 9$. We use two concatenated $X/2$ gates to prepare the qubit in $|1\rangle$. Values in parenthesis, if available, are one standard deviation.

	Q_1	Q_2	Q_3	Q_4	Q_5	Q_6	Q_7	Q_8	Q_9	Q_{10}
$\omega_j^0/2\pi$ (GHz)	5.782	5.831	5.828	5.780	5.760	5.863	5.780	6.004	5.893	5.930
$\omega_I/2\pi$ (GHz)	≈ 5.655									
$T_{1,j}$ (μs)	27.2	24.4	10.9	15.0	19.2	23.7	13.8	11.8	17.1	22.0
$T_{2,j}^*$ (μs)	2.9	2.8	2.8	2.2	2.6	1.8	1.1	2.1	1.7	4.4
$T_{2,j}^{\rm SE}$ (μs)	11.8	10.6	10.0	10.8	11.7	8.9	8.0	8.0	7.9	11.8
$\omega_j/2\pi$ (GHz)	5.080	5.467	5.657	5.042	5.179	5.605	4.960	5.260	5.146	5.560
$g_j/2\pi$ (MHz)	14.2	20.5	19.9	20.2	15.2	19.9	19.6	18.9	19.8	16.3
$X/2$ fidelity	0.9985(2)	0.9992(1)	0.9984(1)	0.9987(2)	0.9991(1)	0.9964(5)	0.9987(1)	0.9980(3)	0.9988(3)	0.9989(1)
Simu. $X/2$ fidelity	0.9978(7)	0.9980(2)	0.9953(5)	0.9955(5)	0.9985(2)	0.9962(3)	–	–	0.9979(2)	0.9931(12)
$\omega_j^r/2\pi$ (GHz)	6.509	6.541	6.615	6.614	6.635	6.694	6.691	6.794	6.809	6.891
$g_j^r/2\pi$ (MHz)	41.3	39.9	40.6	38.2	38.5	40.4	41.8	40.9	40.2	38.7
$\delta\omega_j^m/2\pi$ (MHz)	31.1	32.7	21.1	46.5	9.0	45.1	22.5	19.5	26.0	70.2
n_j^r	92	59	31	180	30	81	93	74	103	203
$1/\kappa_j^r$ (ns)	291	275	272	348	223	284	248	266	299	242
$F_{0,j}$	0.921	0.955	0.982	0.974	0.962	0.988	0.950	0.970	0.961	0.971
$F_{1,j}$	0.867	0.915	0.904	0.928	0.927	0.917	0.922	0.880	0.894	0.934

connecting to the 1st two-tone xy channel, Q_3 and Q_4 share Q_3's on-chip xy line connecting to the 2nd two-tone xy channel, and Q_6 and Q_7 share Q_7's on-chip xy line connecting to the 3rd two-tone xy channel. For the two-tone xy signals that are supposed to simultaneously act on the two qubits, we sequentially place two rotation pulses, each with a single tone targeting one of the two qubits. Each $\pi/2$-rotation (π-rotation) pulse is 30 (60) ns-long with a full width half maximum of 15 (30) ns. We perform randomized benchmark (RB) on the two qubits simultaneously, and verify that overlapping in time the two rotation pulses through the two-tone xy channel is not a problem except for Q_6 and Q_7, which might be due to the large sideband used for Q_7.

The idle frequencies ω_j of the 10 qubits are detuned from each other to minimize the microwave crosstalk during single-qubit rotations. For two qubits sharing the same xy line, the cross-resonance interaction reported elsewhere [S3] is not a major factor due to the large detuning. For each qubit, we optimize the quadrature correction term with DRAG coefficient α to minimize leakage to higher levels [S4], yielding the $X/2$ ($\pi/2$ rotation around the x axis) gate fidelities no less than 0.998 for all 10 qubits as verified by RB on each qubit (Tab. S1 and in Fig. S1). We also select eight qubits and simultaneously perform RBs on them (see pulse sequences in Fig. S2(a)), finding that the $X/2$ gate fidelities remain reasonably high, no less than 0.993 (Q_7 is not selected due to the above-mentioned large sideband issue; Q_8's DAC control has a smaller memory, with a maximum sequence length only half of the others'). We also perform RB simultaneously with shorter pulse sequences (smaller m-Number of gates) on Q_8 and Q_9, two neighboring qubits with the idle frequencies being very close, and find that the $X/2$ gate fidelities remain no less than 0.997.

We note that further optimization of the single-qubit gates are possible by shortening the gate time and introducing a slight detuning to the xy pulse to minimize the phase error [S4]. We carry out the optimization procedure on Q_5 and obtain fidelities of the typical single-qubit gates, X, Y, $\pm X/2$, and $\pm Y/2$, all above 0.999 (Fig. S2(b)).

We note that although single-qubit gates are optimized at the qubits' idle frequencies ω_j, the gate performance may slightly degrade after a big square pulse used to tune the qubit frequency due to the finite rise-up time on the order of a few to a few tens of nanoseconds for an ideally sharp step-edge. In our experiment, after biasing the qubits from the interaction frequency ω_I back to their idle frequencies ω_j, we wait for another 10 ns before applying single-qubit gates. We also use the GHZ tomography data to benchmark the gate fidelities of our $\pi/2$ rotations. For $N = 7$, the density matrix of $|\Psi_1\rangle$ with four major elements in the $|\pm\rangle$ basis has a fidelity of 0.796 ± 0.021. After applying a $\pi/2$ rotation to each qubit we transform $|\Psi_1\rangle$ to $|\Psi_2\rangle$ in the $|0\rangle$ and $|1\rangle$ basis, whose density matrix is measured to exhibit a fidelity of 0.771 ± 0.022 (each 7-qubit full tomography is done within 40 minutes). Therefore we estimate that our $\pi/2$ rotation after the big square pulse for entanglement has an average fidelity around $(0.771/0.796)^{1/7} > 0.995$, while a more detailed numerical simulation suggests that the average $\pi/2$ gate fidelity is > 0.993.

Z control

Our instrument has 10 (expendable to more) independent z signal channels controlled by DACs, which give us the full capability of simultaneously tuning all 10 qubits' resonant frequencies. To correct for the finite rise-up time of an ideally sharp edge of a square pulse, we generate a step-edge output from the DAC and capture the waveform with a high-speed sampling oscilloscope. The measured response of the step-edge gives two time constants describing the response of the room-temperature wirings, based on which we use de-convolution to correct for desired step-edge pulses. Imperfection due to the cryogenic wirings are partially compensated using the qubit's transition frequency response influenced by a step-edge z bias as a caliber [S6].

The effective z bias of a qubit due to a unitary bias applied to other qubits' z lines is calibrated, which yields the z-crosstalk matrix $\tilde{M}_z$ as

$$\begin{bmatrix} 1 & -0.023 & -0.001 & 0.008 & 0.028 & 0.020 & 0.009 & 0.011 & 0.003 & -0.008 \\ -0.018 & 1 & 0.050 & 0.024 & 0.008 & 0.003 & 0.000 & -0.002 & 0.005 & -0.016 \\ -0.021 & -0.081 & 1 & 0.054 & 0.022 & 0.012 & 0.003 & 0.001 & -0.004 & -0.017 \\ 0.017 & 0.055 & 0.080 & 1 & -0.024 & -0.012 & -0.003 & 0 & 0.003 & 0.013 \\ 0.016 & 0.019 & 0.009 & -0.003 & 1 & -0.015 & -0.002 & 0.005 & 0.009 & 0.014 \\ 0.001 & -0.002 & -0.004 & -0.005 & -0.025 & 1 & 0.009 & 0.022 & 0.013 & 0.004 \\ 0.001 & 0 & -0.003 & -0.006 & -0.028 & -0.046 & 1 & 0.078 & 0.035 & 0.008 \\ -0.004 & 0 & 0.001 & 0.003 & 0.013 & 0.020 & 0.025 & 1 & -0.029 & -0.006 \\ -0.012 & -0.006 & -0.002 & 0 & 0.008 & 0.015 & 0.016 & 0.065 & 1 & -0.014 \\ 0.002 & 0.011 & 0.015 & 0.015 & 0.029 & 0.023 & 0.010 & 0.008 & -0.011 & 1 \end{bmatrix}. \quad \text{(S1)}$$

With the z biases applied to the 10 qubits written in a column format as $\tilde{z}_{\text{applied}}$ and the actual z biases sensed by these 10 qubits written as $\tilde{z}_{\text{actual}}$, we have the mapping relation of $\tilde{z}_{\text{actual}} = \tilde{M}_z \cdot \tilde{z}_{\text{applied}}$. The z crosstalks reach maximum at about 8% between two neighboring qubits. We note that the z crosstalks may not contribute to the GHZ state errors as we iteratively fine-tune the z bias of each qubit within a small range for optimal GHZ entanglement.

Qubit readout

Besides the above-mentioned 7 xy signal channels for the qubit control, our instrument has an xy signal channel that can output a readout pulse with multiple tones achieved by sideband mixing; this readout pulse is captured by a room-temperature analog digital converter (ADC), which simultaneously demodulates the multiple tones and returns a pair of I and Q values for each tone. An impedance-transformed Josephson parametric amplifier (JPA) operating at 20 mK is used before

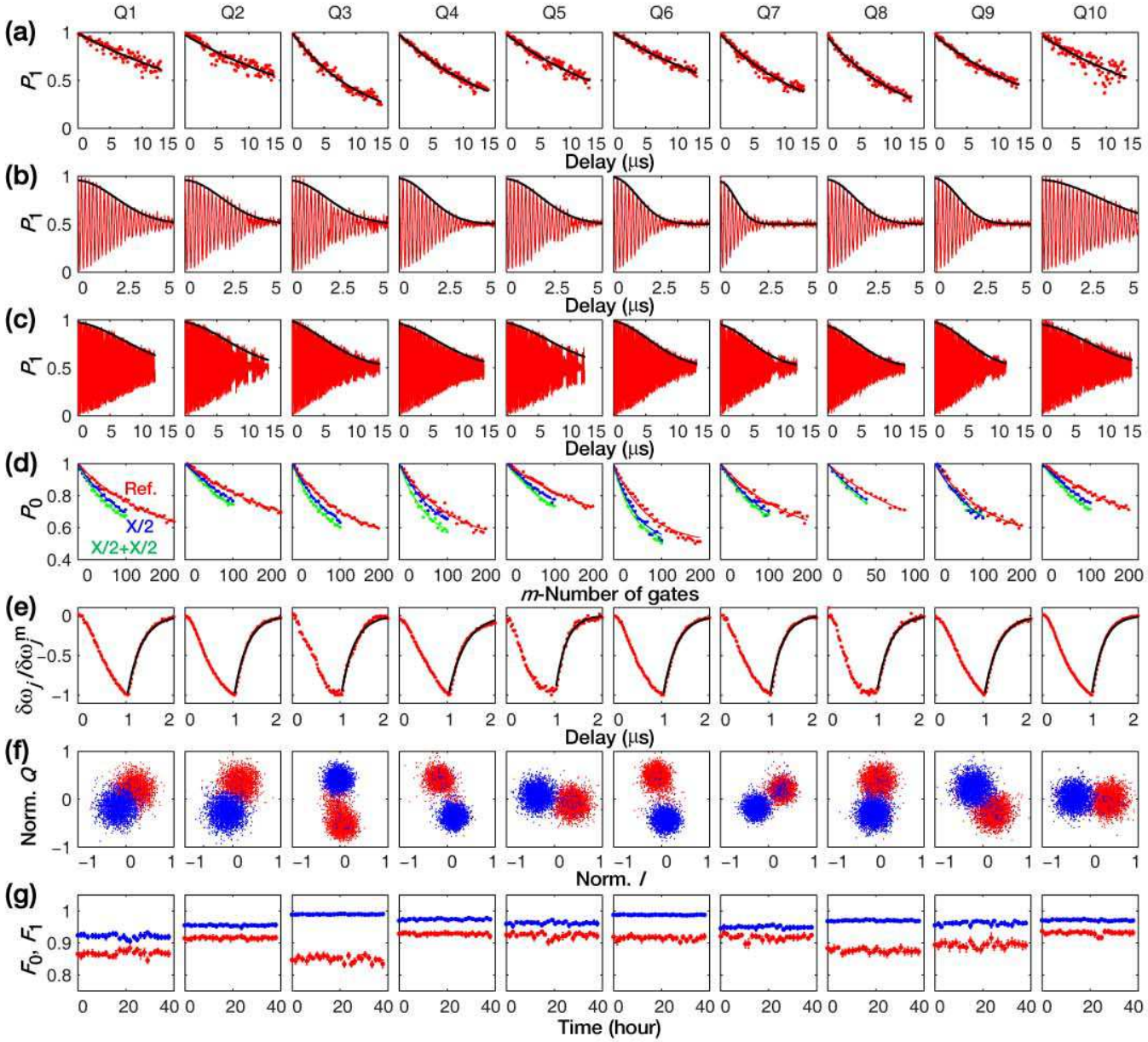

FIG. S1: **Qubit characteristics.** (a) Qubit energy decay measurement (red dots) with its $|1\rangle$-state probability, P_1, corrected as a function of the decay time, t. Black lines are fits according to $P_{1,j} \propto \exp\left(-t/T_{1,j}\right)$ for Q_j. (b) Qubit Ramsey interference measurement (red dots), where the delay time t is between two $\pi/2$ pulses. We fit the envelope of Q_j's Ramsey fringe with $P_{1,j}^{\rm Env} - 0.5 \propto \exp\left[-t/2T_{1,j} - \left(t/T_{2,j}^*\right)^2\right]$. (c) Qubit spin echo measurement (red dots), where an additional π pulse is inserted in the middle of the delay time t compared with the Ramsey sequence. We fit the envelope of Q_j's interference fringe with $P_{1,j}^{\rm Env} - 0.5 \propto \exp\left[-t/2T_{1,j} - \left(t/T_{2,j}^{\rm SE}\right)^2\right]$. (d) RB characterizing the $X/2$ and $X/2 + X/2$ gates. Shown are the $|0\rangle$-state probabilities averaged over $k = 20$ sequences for the reference (red), the $X/2$ gates interleaved with the reference (blue), and the $X/2 + X/2$ gates interleaved with the reference (green) as functions of the m-Number of gates. Probability values drop exponentially with m due to the randomized accumulation of gate-specific errors. Dots are experimental data and lines are fits. (e) The normalized AC stark shift during the qubit-state measurement (see $\delta\omega_j^m$'s value in Tab. S1). Two consecutive readout pulses are used in this experiment following procedures described elsewhere [S5]. Black lines are exponential fits giving the photon leakage rates κ_j^r. (f) The shifted and normalized I-Q data for single-shot qubit-state differentiation, where blue (red) dots are measured I-Q values when qubit is prepared in $|0\rangle$ ($|1\rangle$). There are 3000 dots (repetitions) for each color (qubit state). Q_3's I-Q data apply to the entangling experiments with $N \leq 9$. (g) Qubit $|0\rangle$- and $|1\rangle$-state readout fidelities with error bars, $F_{0,j}$ (blue) and $F_{1,j}$ (red), monitored over a 40-hour period. Q_3's readout fidelities apply to the entangling experiment with $N = 10$ as Q_4 is simultaneously measured (see below). We note that $F_{1,j}$ is usually very stable over a period of a few hours, but could vary more than displayed due to random movements of two-level defects and fluctuations of other environmental factors, all of which affect qubit parameters and degrade the gate fidelity for the $|1\rangle$-state generation. As such we have to constantly monitor the system performance and repeat tune-up procedures if necessary.

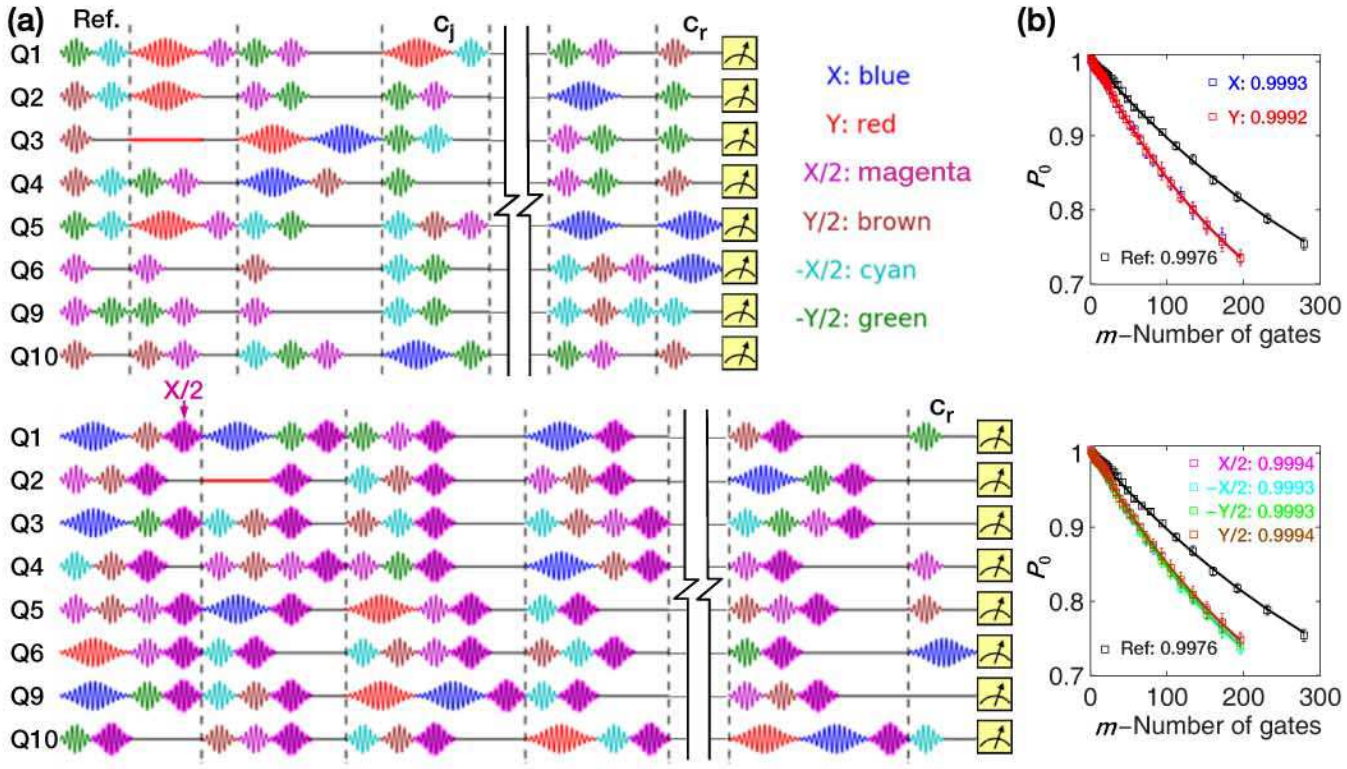

FIG. S2: **Single-qubit RBs.** (a) Pulse sequences for single-qubit RBs running on 8 qubits simultaneously. Top: One representative reference gate sequence. Each sequence has up to m single-qubit Cliffords C_j (divided by vertical dashed lines) and the idling gates, the latter of which are implemented to ensure that the j-th Cliffords on all qubits take the same time slot. Single-qubit rotation gates (sinusoids) used to assemble C_j are color-coded on the right (the I gate is represented by a horizontal red line). The final C_r gate returns each qubit to $|0\rangle$. At the end of the pulse sequence we measure all 8 qubits simultaneously for 2^8 occupation probabilities, based on which we perform partial trace over other qubits' indices for one piece of data on the target qubit; we sum over all data of $k = 20$ random pulse sequences for an exponential fit. Bottom: One representative gate sequence with the $X/2$ gates (bold magenta sinusoids) inserted. On average, each single-qubit Clifford C_j consists of 0.375 gates from X, Y, and I, 1.5 gates from $\pm X/2$ and $\pm Y/2$, and approximately 1 idling gate to ensure synchronization among qubits. Pulse lengths of the X, Y, and I gates are 60 ns; lengths of the $\pm X/2$ and $\pm Y/2$ gates are 30 ns; length of the idling gate for synchronization is 30 ns. In total the average duration of a single-qubit Clifford is about 98 ns. (b) Single-qubit RBs for Q_5 ($k = 30$), where we shorten the pulse length to 20 ns, set $\alpha = 0$, and optimize the detuning to be -0.37 MHz. All single-qubit gate fidelities are above 0.999.

the ADC to enhance the signal-to-noise ratio. The JPA was fabricated as described elsewhere [S1], whose signal-line impedance is continuously varied, in a manner of the Klopfenstein taper, to transform the environmental characteristic impedance from 50 to 15 Ω for a bandwidth of more than 200 MHz centered around 6.72 GHz. The JPA can be switched "ON" and "OFF" by turning on and off, respectively, an appropriate pump tone that is about twice the signal frequency. The signal transmission spectra with the JPA in the states "ON" (red line) and "OFF" (blue line) are displayed in Fig. S3, where the 10 dips correspond to the 10 readout resonators. The amplification band of the JPA, identified by the vertical difference between the red and blue lines, is tunable with a DC bias applied to the JPA.

The readout pulse is 1 μs-long, with the input tones and the power at each tone optimized for high-fidelity readout. The j-th tone of the readout pulse, where j is up to 10 in this experiment, populates Q_j's readout resonator R_j with an average photon number of n_j^r in 1 μs, which dispersively interacts with Q_j with the coupling strength g_j^r and shifts Q_j's frequency downwards by an amount of $\delta\omega_j^m$. Reversely, the qubit state affects the state of its readout resonator, which is encoded in the I-Q values at the tone j of the transmitted readout pulse. At the end of 1 μs, photons in Q_j's readout resonator leak into the circumferential transmission line at the rate of κ_j^r, and the readout resonator returns to the ground state before the next sequence cycle starts.

Repeated readout signals amplified by the JPA are demodulated at room temperature, yielding the I-Q points at each tone on the complex plane forming two blobs to differentiate the states $|0\rangle$ and $|1\rangle$ of each qubit (see Tab. S1 and in Fig. S1). The probabilities of correctly

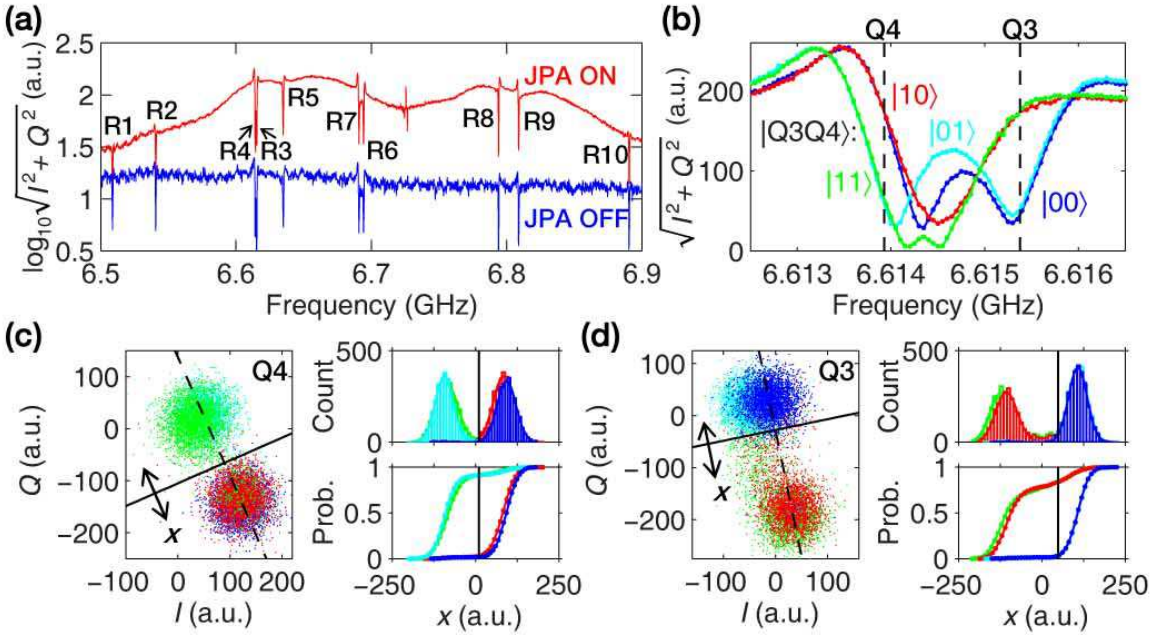

FIG. S3: **Multiqubit readout.** (a) Signal transmission spectra while all qubits are in $|0\rangle$. Shown are the amplitudes of the demodulated signal as functions of signal frequency when the JPA is "ON" (red) and "OFF" (blue). All readout resonators, labeled from R_1 to R_{10}, are visible as dips on the spectra (R_3 and R_4 are very close). The vertical difference between the red and blue lines manifests the JPA's capability of amplifying signals. (b) Detailed signal transmission spectra when Q_3 and Q_4 are prepared in one of the four computational states of $|00\rangle$ (blue), $|01\rangle$ (cyan), $|10\rangle$ (red), and $|11\rangle$ (green). It is possible to differentiate both qubits' state if the readout tones and powers are properly chosen as indicated by the vertical dash lines. (c) Left panel: Demodulated I-Q data of Q_4 when Q_3 and Q_4 are prepared in one of the four computational states (color-coded as in **b**). Top-right panel: Distribution histogram along the x axis as defined by the dash line in the left panel. The vertical line indicates the separatrix to differentiate $|0\rangle$ and $|1\rangle$. Bottom-right panel: Measurement visibility by integrating the histogram data along the x axis. (d) Readout of Q_3 when Q_3 and Q_4 are prepared in one of the four computational states (color-coded as in **b**). The readout crosstalk is visible in the left panel of **d**. But the relative movement of Q_3's $|0\rangle$-state blobs depending on Q_4 in $|0\rangle$ (blue blob) and in $|1\rangle$ (cyan blob) are almost vertical to the x axis, and so are Q_3's $|1\rangle$-state blobs. Therefore Q_4's effect on Q_3 is negligible with our choice of the solid dividing line for state differentiation. The readout tone used for Q_3 here is slightly different from that used when Q_4 is not measured. With this choice Q_3's readout fidelity slightly decreases, but we have verified that with the readout correction we can prepare various product states of Q_3, Q_4, and Q_5 with high-fidelity single-qubit gates, and perform one- and two-qubit state tomography, with the fidelities of all reconstructed density matrices being around or above 0.99.

reading out each qubit in $|0\rangle$ and $|1\rangle$ are listed in Tab. S1.

We note that the readout resonators of Q_3 and Q_4 are very close in frequency, and so are those of Q_6 and Q_7. We carefully choose the readout tones and powers to minimize the readout crosstalk if Q_3 and Q_4 are both being measured, which has a slight side-effect that the readout visibility of Q_3 drops a little bit compared with the case when Q_4 is not being measured (Fig. S3). Nevertheless, our readout choice for minimizing the crosstalk is fully verified by preparing various product states of Q_3, Q_4, and Q_5 with high-fidelity single-qubit gates and performing single- and two-qubit state tomography, with the fidelities of all reconstructed density matrices being around or above 0.99.

XX-type crosstalk coupling

Due to insufficient crossover bonding wires to tie the ground segments on-chip, we experience unwanted microwave crosstalk coupling between nearest-neighbor qubits. The crosstalk coupling is calibrated by measuring the qubit-qubit energy swap process around the interaction frequency ω_I.

To understand the crosstalk coupling, we measure in detail the energy swap process of Q_8 and Q_9 as a function of the qubit detuning from the resonator ω_B, with the result shown in Fig. S4(a) (Q_8 and Q_9 are chosen since they are the nearest-neighbor qubits with two highest sweetpoint frequencies ω_8^0 and ω_9^0): We excite Q_8 to $|1\rangle$ and then detune both Q_8 and Q_9 simultaneously to the same detuning Δ from the resonator, with Δ being varied; by subsequently monitoring the $|1\rangle$-state population of Q_8, P_1, as a function of the interaction time, we

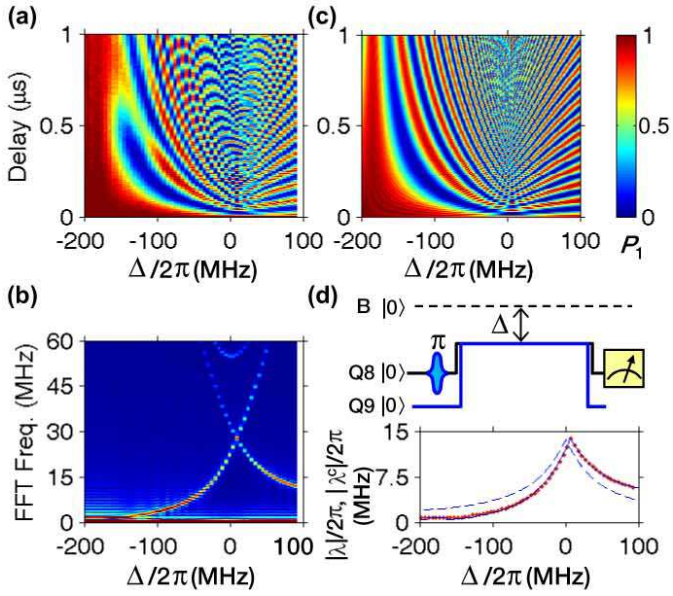

FIG. S4: Q_8-Q_9**'s energy-swap dynamics showing the qubit-qubit interaction including the contribution from the neighboring** XX**-type crosstalk.** After pumping Q_8 to $|1\rangle$, we detune Q_8 and Q_9 both to Δ for a time of delay. Q_8 is measured afterwards. (a) Measured P_1 as a function of both Δ (x axis) and delay (y axis). (b) Fourier transform of the data in **a** along the y axis. (c) Numerical simulation of the measurement in **a** taking into account the XX-type crosstalk interaction. (d) Top: Pulse sequence for the measurement in **a**. Bottom: Amplitude of the total interaction (dots) as a function of Δ obtained from the lower branch in **b**. For comparison, the interaction from the Fourier transform of the numerical data in **c** (solid line) and the theoretical SE strength λ (dashed line) are also illustrated. The SE interaction changes sign across $\Delta = 0$, so that the net qubit-qubit interaction amplitude is antisymmetric.

obtain the energy-swap dynamics of the system at various detunings. The qubit-qubit interaction strength can be inferred from the oscillation period of P_1.

We find that, in addition to the resonator mediated SE coupling λ (see Eq. (2) of the main text) which changes sign across ω_B, a direct XX-type coupling with a magnitude of $\approx 2\pi \times 2.1$ MHz, named as $\lambda^c_{8,9}$ for Q_8-Q_9, must be taken into account to explain our experimental data. Figure S4(b) shows the Fourier transform of the data in Fig. S4(a) along the y axis, based on which the net qubit-qubit interaction as a function of Δ can be inferred, as shown in Fig. S4(d). Overall the experimental data agree well with the numerical simulation taking into account the extra XX-type coupling λ^c (Figs. S4(c) and (d)). The XX-type crosstalk couplings $\lambda^c_{j,j'}$ between other nearest-neighbor qubits (Q_j and $Q_{j'}$) are roughly estimated as the differences between the measured qubit-qubit coupling strengths and theoretical SE interaction strengths, as given in Tab. S2.

Here numerical simulation is based on the Hamiltonian shown in Eq. (1) of the main text with the additional nearest-neighbor crosstalk coupling term $\sum_{j,j'} \lambda^c_{j,j'} \left(\sigma_j^- \sigma_{j'}^+ + \sigma_j^+ \sigma_{j'}^-\right)$, while the decoherence impact is included using the Lindblad master equation taking into account the Markovian environment.Two characteristic decay times, the energy relaxation time T_1 and the pure dephasing time T_φ, are used for each qubit. However, the non-Markovian $1/f$ character of the phase noise prevents us from directly using the $T^*_{2,j}$ values listed in Tab. S1. Empirically we find that using $T_\varphi \geq 10T^*_{2,j}$ ensures that the numerical results agree reasonably well with the data in the first few hundred nanoseconds (note that our GHZ sequences times are less than 150 ns).

TABLE S2: Nearest-neighbor XX-type crosstalk couplings.

	Q_1-Q_2	Q_2-Q_3	Q_3-Q_4	Q_4-Q_5	Q_5-Q_6
$\lambda^c_{j,j'}/2\pi$ (MHz)	1.7	2.6	2.3	2.2	0.2
	Q_6-Q_7	Q_7-Q_8	Q_8-Q_9	Q_9-Q_{10}	Q_{10}-Q_1
$\lambda^c_{j,j'}/2\pi$ (MHz)	2.2	2.3	2.1	2.1	0.06

The estimated XX-type nearest-neighbor couplings are included during the numerical optimization of the parameters for generating GHZ states. It is find that the introduction of the crosstalk couplings lowers the GHZ fidelities for $N > 6$ but actually raises the fidelity for $N = 10$.

MULTIQUBIT GHZ PHASE CALIBRATION

For the multiqubit GHZ entanglement, it is critical that the phase of each qubit's xy drive is calibrated according to the rotating frame at ω_I, after taking into account the extra dynamical phases accumulated during the frequency adjustment of all qubits. Here we follow the approach as done previously [S7]: For simplicity we consider the product state of two qubits as $\frac{1}{\sqrt{2}}(|0\rangle + |1\rangle) \otimes \frac{1}{\sqrt{2}}\left(|0\rangle + e^{i\varphi}|1\rangle\right)$, where the extra φ on the second qubit is seen right after the two qubits are placed on-resonance at ω_I; we intend to find a way to adjust φ to be zero. With the interaction Hamiltonian as $\hbar\lambda(|01\rangle\langle 10| + |10\rangle\langle 01|)$ (see Eq. (2) of the main text), the amplitudes of $|01\rangle$ and $|10\rangle$ then oscillate in time, as described (in the rotating frame) by the unitary transformation $U_{\rm int} = \begin{bmatrix} 1 & 0 & 0 & 0 \\ 0 & \cos(\lambda t) & -i\sin(\lambda t) & 0 \\ 0 & -i\sin(\lambda t) & \cos(\lambda t) & 0 \\ 0 & 0 & 0 & 1 \end{bmatrix}$. At $t = \pi/4|\lambda|$, where λ is negative, the two-qubit state evolves to $|00\rangle/2 + (e^{i\varphi} + i)/(2\sqrt{2})|01\rangle + (ie^{i\varphi} + 1)/(2\sqrt{2})|10\rangle + e^{i\phi}|11\rangle/2$, which gives equal probabilities for the four two-qubit computational states with $\varphi = 0$.

Experimentally we choose Q_3 as the reference and adjust the phase of the other qubit's microwave; we perform the check pairwisely, with the data after all phase cali-

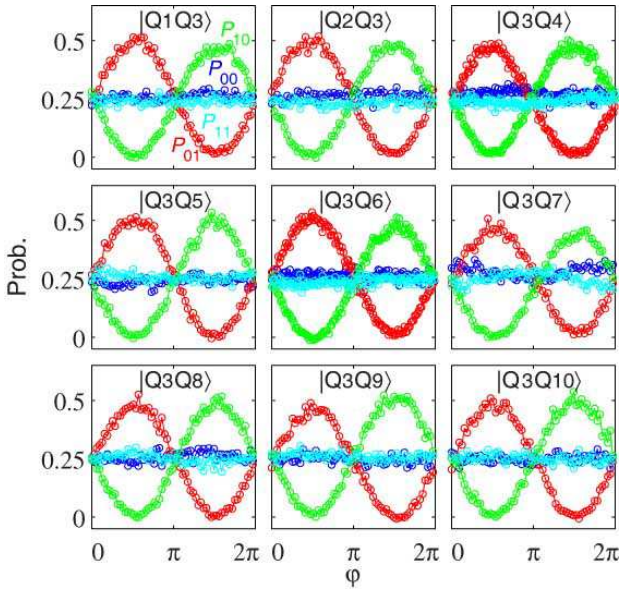

FIG. S5: **Pairwise phase calibrations with Q_3 as the reference.** After driving both qubits with the $\pi/2$ microwave pulses, we tune them to ω_I for an interaction time of $t = \pi/4|\lambda|$, where λ is the net qubit-qubit interaction at ω_I. Afterwards the two-qubit occupation probabilities are measured. For the two $\pi/2$ microwave pulses, we vary the phase φ of the second qubit's microwave for the data shown in each panel with the qubit order as displayed. The occupation probabilities, P_{00} (blue), P_{01} (red), P_{10} (green), and P_{11} (cyan), as functions of φ are shown after the phases of all qubits' microwaves referenced to Q_3's are corrected.

brations shown in Fig. S5.

10-QUBIT TOMOGRAPHY

Effect of reduced sample size

The N-qubit tomography takes 3^N tomographic operations, and for each operation 2^N occupation probabilities of the N-qubit computational states are measured. Once a GHZ state is generated, a tomographic operation is appended, following which the single-shot measurement yields a binary outcome for each qubit and for N qubits simultaneously; running the whole pulse sequence, which includes the state preparation, the tomographic operation, and the measurement, once is one sampling event. Therefore a sufficiently large sample size, i.e., repeating the same pulse sequence many times for many synchronized binary outcomes of all N qubits, is necessary to precisely count all 2^N probabilities, which would significantly slow down the measurement. For the multiqubit tomography, we maintain a fixed sample size of 3000, which is only about 3 times 2^N when $N = 10$; even in this case the full tomography measurement takes about 40 hours if uninterrupted, and we have to constantly monitor our measurement to ensure that the system performance is reasonably stable (Fig. S1). We note that for $N = 10$ a huge number (3^{10}) of operations are involved, resulting in a set of over-constrained equations to solve for the system's density matrix, which may overcome the shortage of an insufficient sample size.

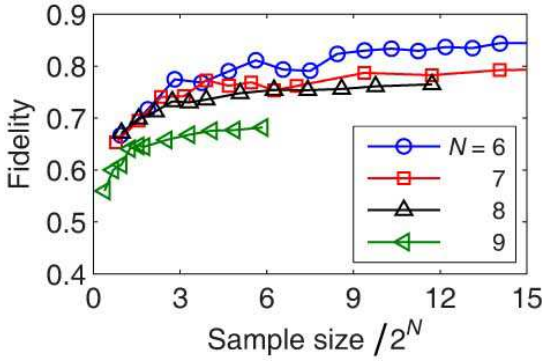

FIG. S6: **Tomography with reduced sample size.** Fidelities of reconstructed density matrices as functions of sample size for $N = 6$ to 9. The data points for different sample sizes on the same line with a fixed N value are sampled from one measurement done with a fixed sample size of 3000: A queue of 3000 simultaneous binary outcomes of N qubits are returned during the measurement, based on which we randomly pick up the desired number (a specified sample size) of outcomes from the queue and calculate the probabilities; the probabilities are then used to infer the density matrix at the specified sample size. During this experiment the state-generation pulse sequences may not be tuned to the optimal.

Furthermore, we carry out a test by performing the N-qubit tomography with a variable sample size for $N = 6$ to 9. The results show that, with the sample size around 3×2^N, the reconstructed density matrix has a fidelity very close to that with a sufficiently large sample size (Fig. S6).

Reducing the computation complexity

Here we use the unitary matrix U^j to describe the j-th tomographic operation on the N-qubit system whose density matrix is ρ, where both U^j and ρ are of size $2^N \times 2^N$. The measured probability of the k-th computational state after the tomographic operation is therefore

$$P_k^j = \langle k|U^j \rho \left(U^j\right)^\dagger |k\rangle = \sum_{l,m=1}^{2^N} U_{kl}^j \left(U_{km}^j\right)^* \rho_{lm}, \quad \text{(S2)}$$

where $k = 1$ to 2^N indexes the N-qubit computational states. Vectorization of the matrix ρ by stacking its columns into a single column vector $\tilde{\rho}$, we have $\tilde{P}^j = \tilde{U}^j \tilde{\rho}$, where $\tilde{P}^j$ is the vector format of $\{P_1^j, P_2^j, \ldots, P_N^j\}$ and $\tilde{U}^j$ is a $2^N \times 4^N$ matrix replacing the summation terms of U_{kl}^j and $(U_{km}^j)^*$ in Eq. (S2). Stacking all tomographic

operation matrices $\tilde{U}^j$ and all measured probabilities $\tilde{P}^j$ for $j = 1$ to 3^N into $\tilde{U}$ and $\tilde{P}$, respectively, we obtain the linear equations of $\tilde{U}\tilde{\rho} = \tilde{P}$, which is used to solve for $\tilde{\rho}$ given $\tilde{P}$ and $\tilde{U}$.

$\tilde{U}$ is a column full rank matrix of size $6^N \times 4^N$. When N approaches 10, it becomes extremely difficult to fully load $\tilde{U}$ into a computer's memory and solve for $\tilde{\rho}$. Fortunately, only a small fraction of $\tilde{U}$'s elements are non-zero, so that we can use sparse matrix for storage and employ the pseudo-inverse method. With $\tilde{U}^\dagger$ as the Hermitian conjugate of $\tilde{U}$, we have $\tilde{U}^\dagger\tilde{U}\tilde{\rho} = \tilde{U}^\dagger\tilde{P}$, where $\tilde{U}^\dagger\tilde{U}$ is a symmetric and positive definite matrix of size $4^N \times 4^N$. $\tilde{U}^\dagger\tilde{U}$ is not only smaller in size, but also more sparse than $\tilde{U}$, which greatly reduce the complexity when solving the equations.

Here we quote the time complexity to quantitatively describe the advantage of using $\tilde{U}^\dagger\tilde{U}$. For a general full rank matrix of size $4^N \times 4^N$, the time complexity involved in computing the inverse operation is $O\left(\left(4^N\right)^3\right)$. For comparison, $\tilde{U}^\dagger\tilde{U}$ has non-zero elements only at the indices of $\left[(k-1)\times 2^N + k + l,\, 1 + l\right]$ and $\left[1 + l,\, (k-1)\times 2^N + k + l\right]$, where $k = 1, 2, \ldots, 2^N$ and l can be any non-negative integers for the indices to be valid. The number of non-zero elements in each row of $\tilde{U}^\dagger\tilde{U}$ is less than 2^N, and thus the number of column elementary operations needed for each row is less than 2^N during matrix inversion; the total number of operations for the 4^N rows is less than $2^N \times 2^N \times 4^N$. We conclude that the time complexity of solving the inverse matrix of $\tilde{U}^\dagger\tilde{U}$ is $O\left(\left(4^N\right)^2\right)$.

10-qubit ρ in the $|0\rangle$ and $|1\rangle$ basis

The GHZ density matrix shown in Fig. 3 of the main text has four major elements in the $|\pm\rangle$ basis, while our measurement is in the $|0\rangle$ and $|1\rangle$ basis. Here we show the partial matrix elements for the 10-qubit GHZ density matrix in the $|0\rangle$ and $|1\rangle$ basis. It is seen that all matrix elements of ρ are no higher than 0.003 in amplitude (Fig. S7).

* C. S. and K. X. contributed equally to this work.
† Electronic address: t96034@fzu.edu.cn
‡ Electronic address: xbzhu16@ustc.edu.cn
§ Electronic address: hhwang@zju.edu.cn

[S1] C. Song *et al.*, submitted (2017).
[S2] M. Steffen *et al.*, Science **313**, 1423 (2006).
[S3] J. M. Chow *et al.*, Phys. Rev. Lett. **107**, 080502 (2011).
[S4] J. Kelly *et al.*, Phys. Rev. Lett. **112**, 240504 (2014).
[S5] E. Jeffrey *et al.*, Phys. Rev. Lett. **112**, 190504 (2014).
[S6] M. Hofheinz *et al.*, Nature **459**, 546 (2009).
[S7] Y. P. Zhong *et al.*, Phys. Rev. Lett. **117**, 110501 (2016).

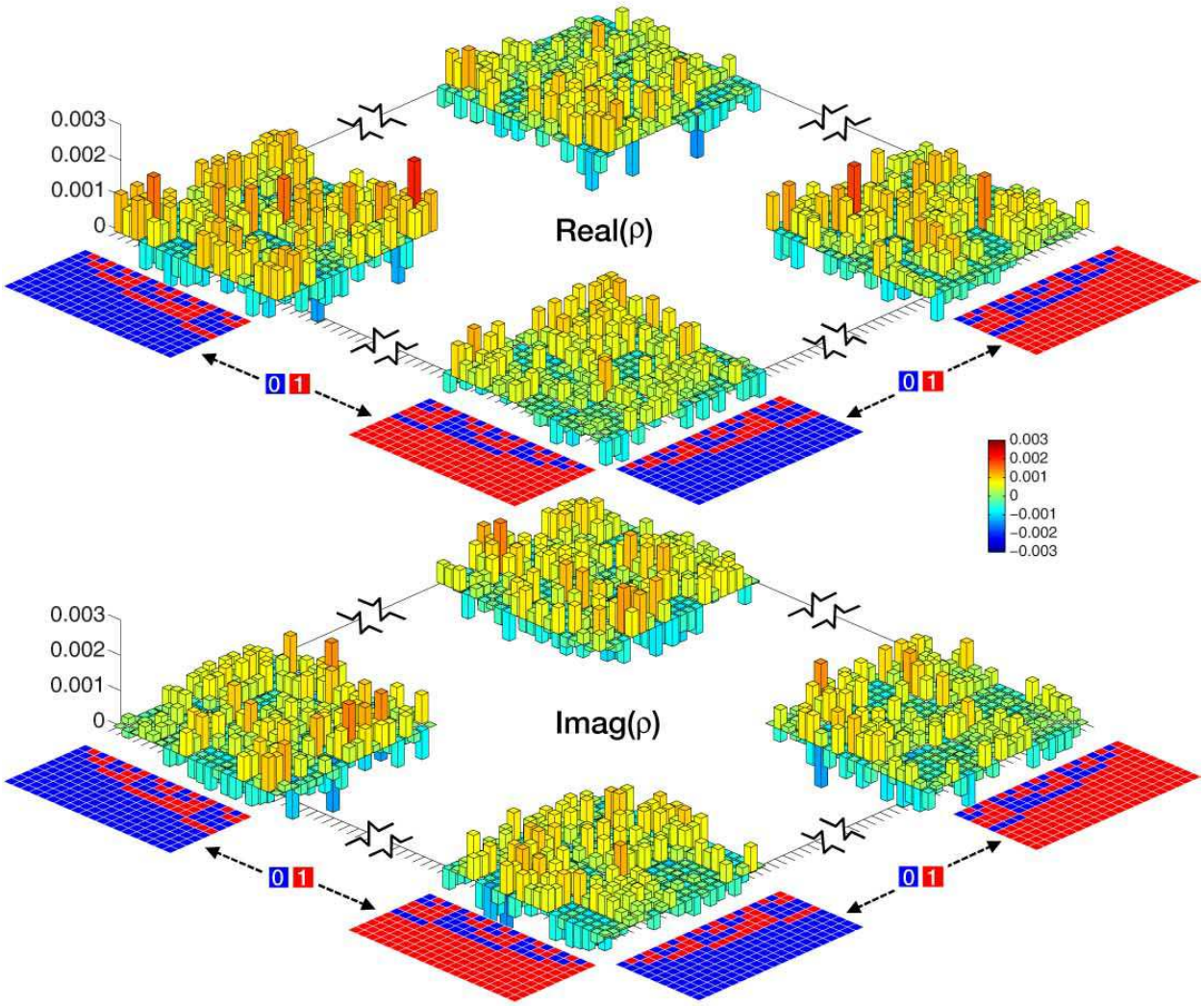

FIG. S7: **10-qubit tomography.** Partial matrix elements for the 10-qubit GHZ ρ in the $|0\rangle$ and $|1\rangle$ basis.